

Article

Synergistic Effect of the KBrO_3 Electron Acceptor on the Photocatalytic Performance of the Nb-TiO₂ Nanocomposite for Polluted Phenol Red Wastewater Treatment

Najla Khaled Almulhem¹, Chawki Awada^{1,*} , Nisrin Mohammed Alnaim¹ , Nada Al Taisan¹ ,
Adil Ahmed Alshoaibi¹  and Nagih M. Shaalan^{1,2,*} 

¹ Department of Physics, College of Science, King Faisal University, P.O. Box 400, Al-Ahsa 31982, Saudi Arabia

² Physics Department, Faculty of Science, Assiut University, Assiut 71516, Egypt

* Correspondence: cawada@kfu.edu.sa (C.A.); nmohammed@kfu.edu.sa (N.M.S.)

Abstract: In this work, the effect of KBrO_3 on the photodegradation mechanism of Nb-TiO₂ nanocomposites was analyzed. The photocatalytic activities of Nb-TiO₂ were evaluated by using a high concentration of phenol red (PR). Nb-TiO₂ nanocomposites were fabricated by a simple sol-gel route with new experimental conditions. HRTEM and EDX were used to study the structural properties of the Nb-TiO₂ nanocomposites. KBrO_3 decreased the degradation time of 20 mg·L⁻¹ of phenol red to 110 min, shorter than that in our previous work without KBrO_3 . In addition, the results showed that the addition of KBrO_3 led to a significant degradation process, which reached an efficiency of 95%. The fast decomposition of the PR pollutants was due to the charge transfer between the KBrO_3 and Nb-TiO₂ nanocomposites in the wastewater treatment.

Keywords: TiO₂ nanoparticles; Nb-TiO₂; KBrO_3 ; electron acceptor; degradation



Citation: Almulhem, N.K.; Awada, C.; Alnaim, N.M.; Al Taisan, N.; Alshoaibi, A.A.; Shaalan, N.M. Synergistic Effect of the KBrO_3 Electron Acceptor on the Photocatalytic Performance of the Nb-TiO₂ Nanocomposite for Polluted Phenol Red Wastewater Treatment. *Crystals* **2022**, *12*, 1758. <https://doi.org/10.3390/cryst12121758>

Academic Editor: Younes Hanifepour

Received: 31 October 2022

Accepted: 1 December 2022

Published: 4 December 2022

Publisher's Note: MDPI stays neutral with regard to jurisdictional claims in published maps and institutional affiliations.



Copyright: © 2022 by the authors. Licensee MDPI, Basel, Switzerland. This article is an open access article distributed under the terms and conditions of the Creative Commons Attribution (CC BY) license (<https://creativecommons.org/licenses/by/4.0/>).

1. Introduction

Growing demand for clean water is a serious concern worldwide, especially in desert areas such as Saudi Arabia, where the sources of clean water are limited. Climate change and increasing population are the primary reasons for this problem. To address the issue, governments are providing more research funding to develop innovative solutions for the purification of water polluted with contaminants, such as inorganic dyes. One of these solutions is to use an advanced oxidation process based on semiconductor photocatalysts.

Due to its important optical and electronic properties, TiO₂ is still one of the best candidates to be used in a variety of applications such as solar cell transport layers, hydrogen production, pollution removal, and CO₂ reduction [1–5]. Using pure TiO₂ without any modification has shown a variety of challenges during its application such its higher recombination rate and wide band gap. Different studies have reported the modification of TiO₂ semiconductors by doping with metal/transition metal [6–13]. For example, in our previous work, Nb/TiO₂ nanocomposites were successfully fabricated and showed a higher photocatalytic activity and a significant shift of the band gap toward the visible wavelength range.

Tuning and engineering the band gap have shown significant effects in increasing the photocatalytic activities of TiO₂ nanocrystals; however, there still remains a need to further increase the photocatalytic activities of the metal/metal transition/TiO₂ nanocrystals using other strategies. One of these strategies is to use the donors/acceptors of electrons during the reaction [14,15]. KBrO_3 was used with metal-supported TiO₂ and showed a significant increase in the synergistic photocatalytic degradation of pyridine [16]. KBr and KI were used at various concentrations and pH values on the photocatalytic degradation of dye W-7G using nanoscaled TiO₂ [17]. TiO₂/UV/H₂O₂, TiO₂/UV/ KBrO_3 , and TiO₂/UV/(NH₄)₂S₂O₈ were used to remove anthraquinone dye Reactive Blue 19 (RB 19)

by heterogeneous advanced oxidation processes under different conditions [18]. Although there has been some research work on the effect of acceptors such as KBrO_3 on metal/ TiO_2 nanocomposites, no work has been reported elsewhere on the effect of acceptors on the new photocatalysts Nb/ TiO_2 nanocomposites reported recently in our work.

In this work, the structural properties of Nb- TiO_2 were investigated using HRTEM and EDX mapping. Two concentrations of KBrO_3 were added to the nanocomposites, a comparison was carried out between that with and without KBrO_3 . The degradation efficiency, concentration decay, and degraded quantity of $20 \text{ mg}\cdot\text{L}^{-1}$ PR with 5.0 mg of the photocatalysts were analyzed under UV-Vis irradiation light.

2. Materials and Methods

2.1. Materials Preparation

TiO_2 nanoparticles were obtained from Skyspring Nanomaterials (product ID: 7930DL, Houston, TX, USA) with an average size of 5 nm. Niobium (V) ethoxide was obtained from Sigma-Aldrich (CAS number 3236-82-6), Schnellendorf, Germany. KBrO_3 , ACS, 99% min, was purchased from Alfa Aesar (CAS number 40013), Kandel, Germany. We added niobium ethoxide in a suspension of TiO_2 nanopowders with a 2% weight ratio of Nb/ TiO_2 ; then, we stirred the solution at $350 \text{ }^\circ\text{C}$ for 30 min. After stirring, we put the obtained gel in a vacuum chamber for dehydration and crystallization for 48 h. Finally, the powders were ground with a mortar to obtain fine powders of Nb(x)/ TiO_2 . For the photocatalysis experiment, 1 mg and 5 mg of KBrO_3 were added to two solutions containing 5 mg of the photocatalysts (Nb- TiO_2), denoted by 20% and 100%, respectively. In this work, we used four samples: pure TiO_2 , Nb- TiO_2 , Nb- TiO_2 with 20 wt.% KBrO_3 , and Nb- TiO_2 with 100 wt.% KBrO_3 . The method is described in detail in our previous work [19].

2.2. Experimental Methods

For the high transmission electronic microscopy (HRTEM) and EDX measurements, the nanoparticles were sonicated for 10 min; then, $5 \mu\text{L}$ of the suspension was deposited on a carbon-coated copper grid. HRTEM and EDX measurements were performed using the instrument (JEOL, JEM-2100F, Tokyo, Japan) operated with 200 kV.

For the photocatalysis measurement, a solution of $20 \text{ mg}\cdot\text{L}^{-1}$ PR was mixed with 5.0 mg of photocatalyst in 50 mL of PR solution. UV-Vis absorbance spectra (Hitachi UV-1800, Reinach, Suisse) spectrophotometers with scanning rates of 5.0 nm/s were used to record the UV-Vis absorbance spectra of phenol red. A 400 W iron-doped metal halide UV bulb in the spectral region 315–400 nm (UV 400 HL230 Fe Clear-A, UV Light Technology Limited, Birmingham, UK) was used for the photodegradation with an intensity of 100 mW/cm^2 . The photodegradation of phenol red was conducted by measuring the variation in the absorbance intensity located at 450 nm.

2.3. Photodegradation of Phenol Red

The photocatalysis was carried out based on the absorbance measured within the wavelength range (350–550 nm). The phenol red concentration was $20 \text{ mg}\cdot\text{L}^{-1}$. In addition to a blank experiment, we carried out an experiment on the phenol red with KBrO_3 , which confirmed the negligible effect of KBrO_3 on the photolysis of PR when exposed to the UV-Vis light. Figure 1 exhibits the absorbance spectra of the effects of the adsorption and photocatalysis on dye degradation. The absorbance spectrum was firstly measured for the pure dye; then, 5 mg of the nanocomposite was placed in a beaker containing 50 mL dye, which was kept for two hours in the dark before starting the photocatalysis effect, see Figure 1. The adsorption (red curve with irradiation time = 0 min) in the dark could be ignored compared to the photocatalysis degradation. After exposing the mixture to the UV-Vis irradiation for 15 min, a large amount of dye was degraded. The degradation amount of the dye was dependent on the nanocomposite type, where the Nb- TiO_2 had faster degradation than the pure TiO_2 . In addition, the Nb- TiO_2 with KBrO_3 had faster degradation activity than the others. After 15 min of irradiation, the absorbance spectra

at the maximum wavelength decreased from 0.15 to 0.10, 0.08, 0.06, and 0.048 for pure TiO₂, Nb-TiO₂, Nb-TiO₂-20%KBrO₃, and Nb-TiO₂-100%KBrO₃, respectively. The results exhibited simultaneously the effect of Nb and KBrO₃ on the photocatalysis activity of the nanocomposites.

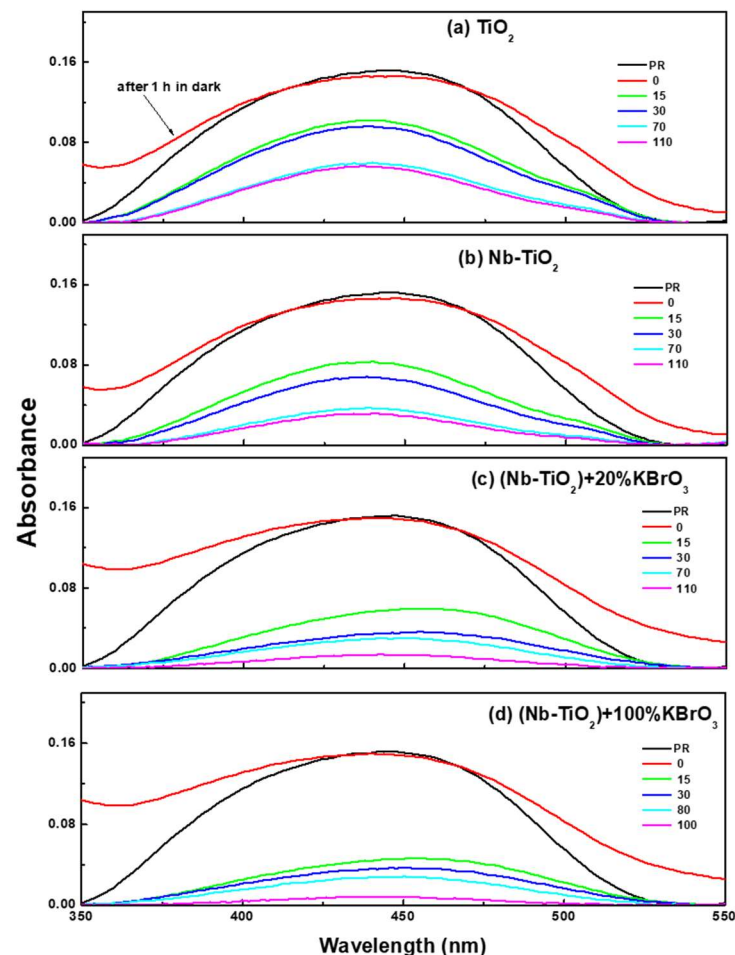


Figure 1. Absorbance spectra by the exposure time for pure TiO₂, Nb-TiO₂, Nb-TiO₂/20%KBrO₃, and Nb-TiO₂/100%KBrO₃.

The absorbance curves of the pure TiO₂ and the Nb-TiO₂/KBrO₃ nanocomposites were used for the calculation of the PR degradation efficiency. Figure 2 shows the PR degradation efficiency with a concentration of 20 mg·L⁻¹ on 5.0 mg of pure TiO₂ and its nanocomposites as a function of the irradiation time. The photodegradation efficiency was estimated based on the following relationship:

$$\eta\% = \frac{C_0 - C_t}{C_0} \times 100 \quad (1)$$

where C_0 and C_t are the initial and instantaneous concentration of the dye at irradiation time, t , respectively. For pure TiO₂ and Nb-TiO₂, the efficiency gradually increased with time reaching 31 and 44%, respectively, in the first 15 min. However, for the Nb-TiO₂/KBrO₃ samples, the efficiency showed higher values by reaching 60 and 70% for 20%KBrO₃ and 100%KBrO₃, respectively. The photodegradation efficiency of the pure TiO₂ and Nb-TiO₂ gradually increased, reaching 64 and 86% after an irradiation time of 110 min. The photodegradation efficiency of Nb-TiO₂/KBrO₃ slowly increased, reaching 92 and 95% after an irradiation time of 110 min.

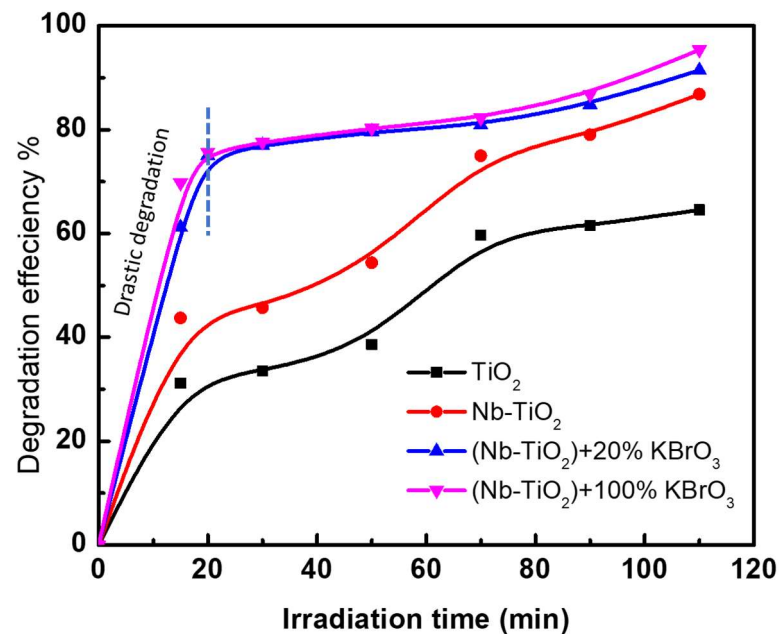


Figure 2. The photocatalytic efficiency of pure TiO₂, Nb-TiO₂, Nb-TiO₂/20%KBrO₃, and Nb-TiO₂/100%KBrO₃.

The maximum of the absorbance spectra was proportional to the dye concentration, where a calibration curve can be carried out. The dye concentration was extracted from the absorbance curve as a function of the irradiation time in terms of mg/L. This curve exhibits the concentration of the phenol red remaining in the solution at each time interval, as shown in Figure 3. For pure and Nb-TiO₂, the concentration decreased from 20 mg/L to 13.7 and 11.2 mg/L, respectively, after 15 min of irradiation. The concentration reached 7.0 and 2.6 mg/L after 110 min of irradiation. A significant improvement occurred for the sample mixed with KBrO₃ at 20%wt and 100%wt compared to the Nb-TiO₂. The dye concentration decreased to 1.6 and 0.8 mg/L, respectively.

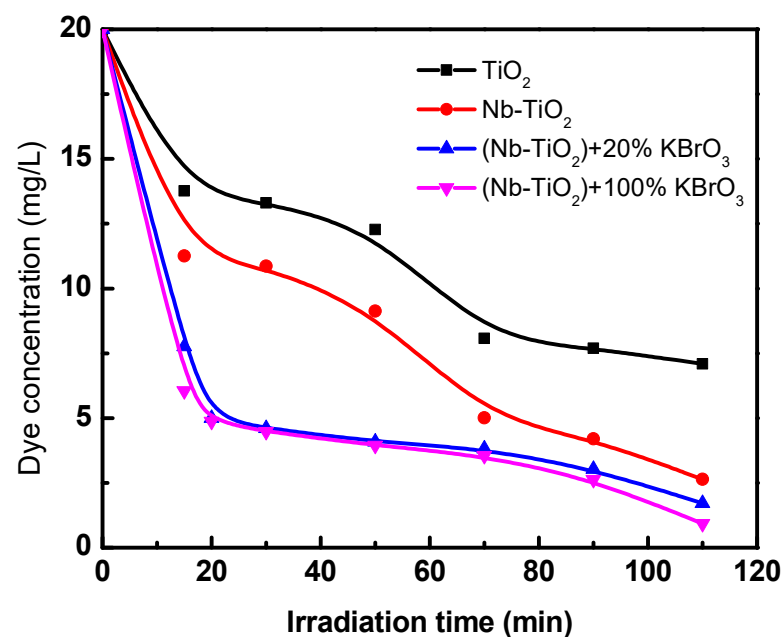


Figure 3. The reduction in the concentration of phenol red dye in the wastewater with irradiation time for pure TiO₂, Nb-TiO₂, Nb-TiO₂/20%KBrO₃, and Nb-TiO₂/100%KBrO₃. Note: the dye concentration was 0.9 mg/L after 110 min for Nb-TiO₂/100%KBrO₃.

3. Results and Discussion

3.1. Structure Analysis of the Nb-TiO₂ Nanocomposites

In order to identify the phase and the structure of the pure TiO₂ and Nb-TiO₂ nanoparticles, we measured the XRD patterns, as shown in Figure 4. Different diffraction peaks appeared, located at 2θ angles 25.3, 37.9, 48.05, 53.9, 55.06, 62.4, 68.76, 70.3, and 75.06 that corresponded to the crystal planes of anatase phase TiO₂ ((101), (004), (200), (105), (211), (204), (116), (220), and (215), see JCPDS card no. 21-1272. We also observed a very weak peak located at 55.96 in Nb-TiO₂ that corresponded to the crystal plane of niobium oxide (102), see JCPDS card No. 30-0873 [20].

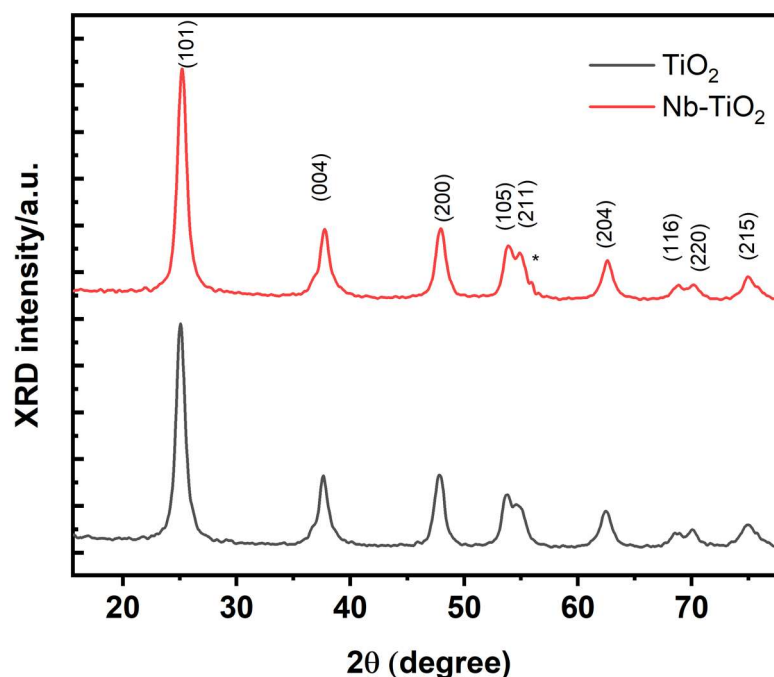


Figure 4. XRD patterns of the TiO₂ and Nb-TiO₂ samples. * represents the peak located at 55.96 in Nb-TiO₂ that corresponded to the crystal plane of niobium oxide (102).

Very small nanoparticles of TiO₂ with an average size of 5 nm were shown in the TEM images (see Figure 5a,b). The nanoparticles with different crystal orientations were observed in the HRTEM images, see Figure 5b. The interplane distance of the (101) plane was 0.33 nm, see Figure 5c. Figure 5d shows the selected area electron diffraction (SAED) pattern corresponding to the rings and the (101), (004), (200), (211), and (204) planes. The first ring marked by a yellow circle corresponded to the (101) plane. Figure 6a–e shows the elemental mapping and energy dispersive spectra of the 5 nm pure TiO₂ nanocomposites. The presence of the Ti and O in the 5 nm TiO₂ nanoparticles is clearly seen. The atomic percentage for O and Ti was 69.88 and 30.12, respectively.

Very small nanoparticles of Nb-TiO₂ with an average size of 5 nm were shown in the TEM images (see Figure 7a,b). The difference from the pure was the dispersion of the nanoparticles. Nanoparticles with different crystal orientations were observed in the HRTEM images, see Figure 7b. The interplane distance of the (004) plane was 0.22 nm, see Figure 7c. Figure 7d shows the selected area electron diffraction (SAED) pattern corresponding to the rings and the (101), (004), (200), (211), and (204) planes. The first ring marked by a yellow circle corresponded to the (101) plane. The first ring marked by a yellow circle corresponded to the (004) plane. Figure 8a–e shows the elemental mapping and energy dispersive spectra of the 5 nm Nb/TiO₂ nanocomposites. The presence of the Ti, O, and Nb in the 5 nm Nb/TiO₂ nanocomposites is clearly seen. The atomic percentage for O, Ti, and Nb was 73.97, 25.94, and 0.09, respectively.

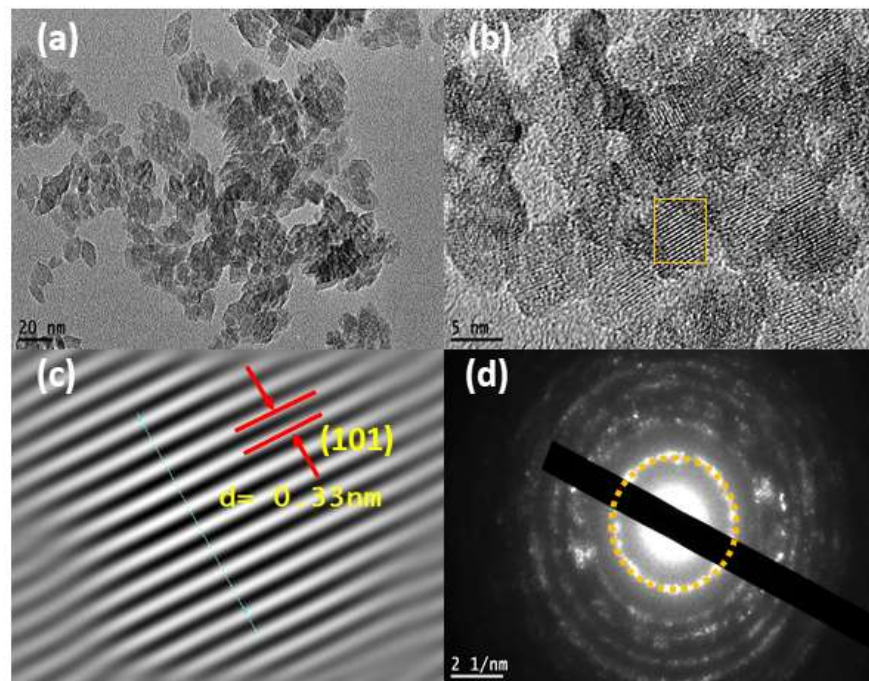


Figure 5. (a,b) TEM images, (c) HRTEM image, and (d) SAED pattern of the 5 nm TiO₂ nanoparticles.

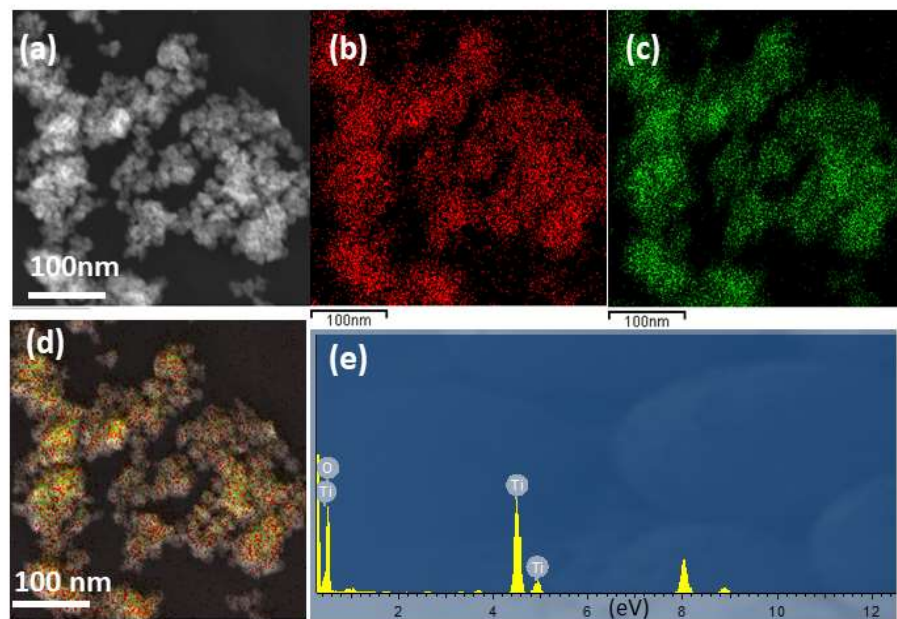


Figure 6. (a) TEM image: (b) dispersivity of O, (c) dispersivity of Ti, (d) elemental mapping of Ti and O, and (e) EDX analysis of 5 nm TiO₂ nanocomposites. The atomic percentage for O and Ti was 69.88 and 30.12, respectively.

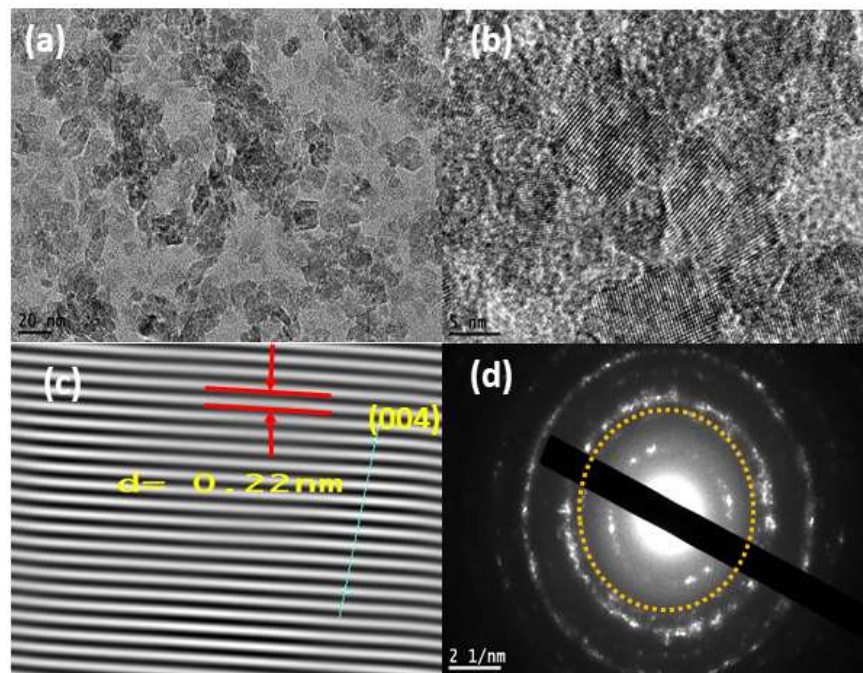


Figure 7. (a,b) TEM images, (c) HRTEM image, and (d) SAED pattern of the 5 nm Nb/TiO₂ nanoparticles.

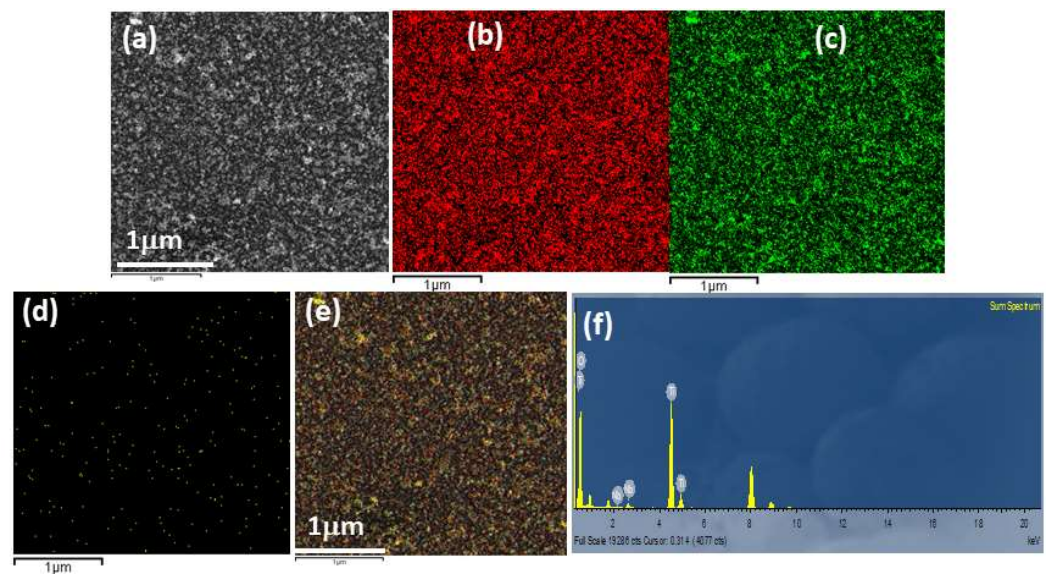
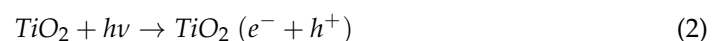


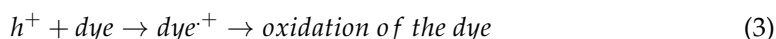
Figure 8. (a, b) TEM images, (c) HRTEM image, and (d) SAED pattern of the 5 nm Nb/TiO₂ nanoparticles, (e) elemental mapping of Ti, O, and Nb and (f) EDX analysis of 5 nm TiO₂ nanocomposites. The atomic percentage for O, Ti, and Nb is 73.97, 25.94, and 0.09, respectively.

3.2. Photocatalysis Mechanism: Effect of the Nb and KBrO₃ Acceptors

The above results can be explained in terms of the photocatalytic mechanism for the phenol red degradation on the Nb-TiO₂ nanocomposite compared to the TiO₂ only and the high performance of the KBrO₃. In general, the photocatalytic phenomenon toward phenol red degradation was defined in the literature based on the advanced oxidation process [21,22]. The dye photolysis in the water begins when the nanocomposite is optically excited, forming an electron-hole pair ($e^- - h^+$), as in Equation (2).



Due to the oxidizing potential of the h^+ , a direct oxidation of the dye may occur, as in Equation (3).



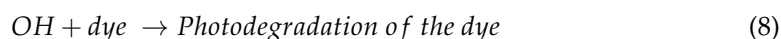
The hydroxyl radical (OH), which is also responsible for photolysis, is formed either by the decomposition of H_2O or by the reaction of OH^- with the holes.



Moreover, the conduction band electrons can react with oxygen molecules, forming peroxide anions, which also produce $\cdot OH$ radicals.



The OH radical was found to be the main cause of mineralizing the organic dye, as indicated in Equation (9). It is well known that the $\cdot OH$ radical is a strong oxidizer with a potential of 2.8 eV.



The data reported in the current study indicated that the Nb-TiO₂ was more reactive toward the degradation of phenol red than the pure TiO₂. This result may be due to the low recombination of the exciting carriers, where the existence of Nb may pick up the excited electrons from the TiO₂ conduction band. In addition, the existence of the electron acceptor KBrO₃ highly improved the photocatalysis activity of this nanocomposite.

In photocatalytic reactions, the most important factor for obtaining high efficiency is the reduction in the e–h recombination. It is said that the main factor wasting energy is the electron–hole recombination, which leads to a lower yield. High efficiency and quantitative yield can be realized by the addition of an electron acceptor to the nanocomposites, such as the KBrO₃ acceptor [16,23]. Some publications have reported that the addition of this electron acceptor improved the efficiency of photolysis. This occurred in our study, where KBrO₃ prevented the recombination of the e–h due to the acceptance of the conduction electrons of the oxide; thus, it led to an increase in the concentration of OH , which led to a rapid degradation of the dye. As shown in Figure 2, the addition of the KBrO₃ increased the photocatalytic degradation to 95% at an irradiation time of 110 min.

These speculations were confirmed by measuring the photocurrent for these four samples at a bias of 0.2 V, as shown in Figure 9. The photocurrent was measured when the samples were irradiated for 60 s. The recorded values of the photocurrent during this interval were 0.65, 1.27, 5.03, and 6.02 μA for TiO₂, Nb-TiO₂, (Nb-TiO₂)/20%KBrO₃, and (Nb-TiO₂)/100%KBrO₃, respectively. The high photocurrent values exhibited the significant effect of the KBrO₃, which helped to extract and collect more electrons during the excitation of Nb-TiO₂, confirming that KBrO₃ is a suitable candidate as an electron acceptor to enhance the photocatalysis properties of this nanocomposite. In Figure 9c,d, we observed that the current continued increasing even after the irradiation was stopped. The existence of the KBrO₃ increased the reaction in Equations (4)–(7). We also observed that the recovery time was slower with the presence of KBrO₃, which was due to the slower recombination rate of the electron–hole.

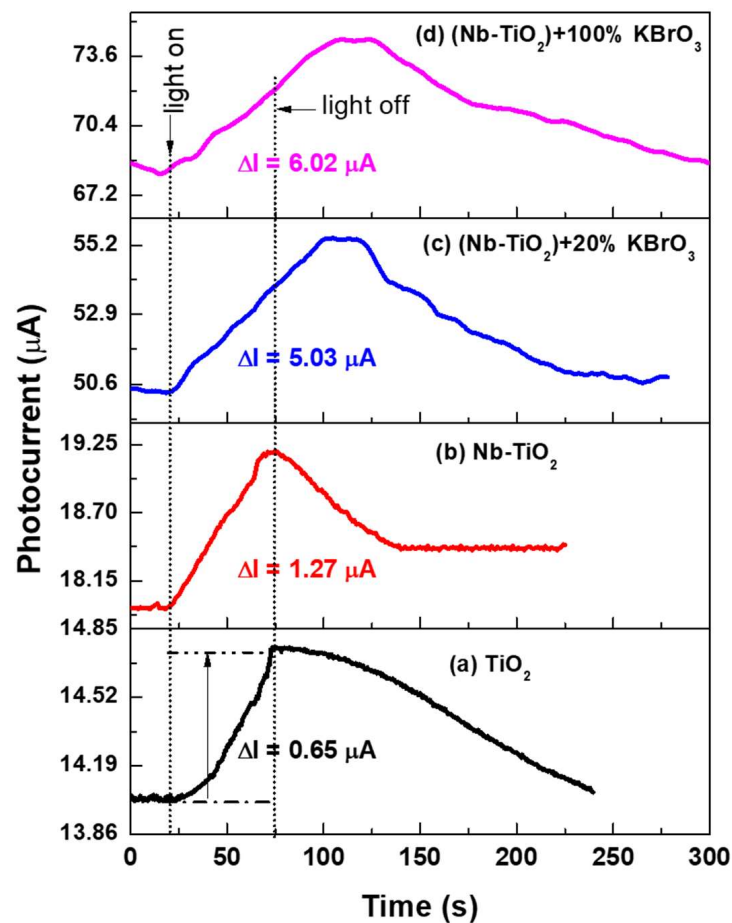


Figure 9. The photocurrent obtained at a bias voltage of 0.2 V for pure TiO_2 , Nb-TiO_2 , $\text{Nb-TiO}_2/20\%\text{KBrO}_3$, and $\text{Nb-TiO}_2/100\%\text{KBrO}_3$.

The data measured for the photodegradation revealed the strong effect of adding Nb to TiO_2 and the significant effect of the KBrO_3 as an electron acceptor in the solution. This can be expressed by calculating the instantaneous quantity (q_t) of the degraded dye, as follows:

$$Q_t = \frac{(C_0 - C_t)}{m} V \quad (9)$$

where m is the adsorbent mass in g , and V is the solution volume in L . The quantity of degraded phenol red increased with the increase in the irradiation time, as shown in Figure 10. This figure indicates the ability of the fast degradation of phenol red on the surface of the oxide. The degradation quantity of the dye reached 191 mg for 1 g of the adsorbent after 110 min for the Nb-doped oxide assisted with KBrO_3 . However, the degradation quantity of the same dye on the pure TiO_2 was 128 mg for the same time. The results exhibited the superiority of the Nb-doped TiO_2 assisted with KBrO_3 to degrade a large quantity of the dye within a short time compared to the TiO_2 .

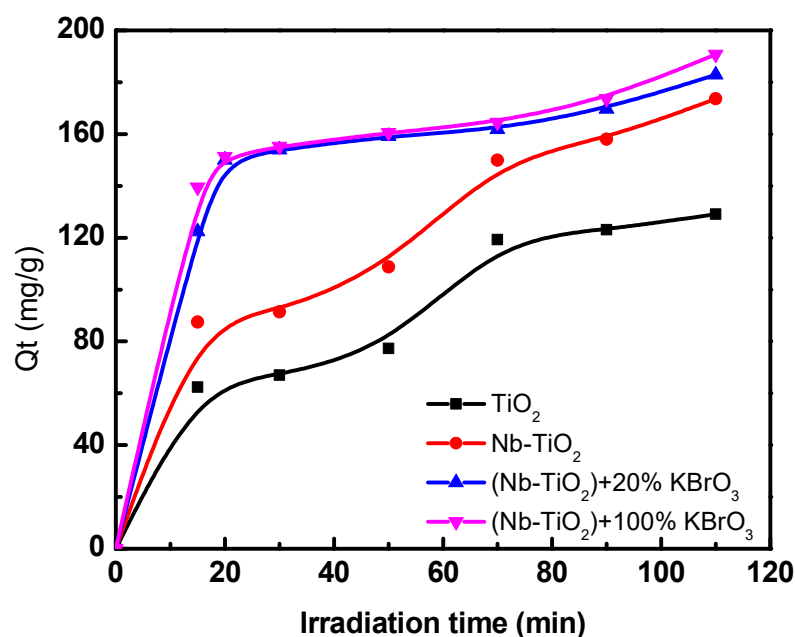


Figure 10. Effect of the degradation quantity of the phenol red concentration as a function of the irradiation time for the pure TiO₂, Nb-TiO₂, Nb-TiO₂/20%KBrO₃, and Nb-TiO₂/100%KBrO₃.

4. Conclusions

A comparison study between the photodegradation efficiency of pure TiO₂, Nb-TiO₂, and KBrO₃/Nb-TiO₂ was successfully performed. The fabricated nanocomposites showed a good degradation of the phenol red with a high concentration of 20 mg/L. The degradation efficiency was increased from 60% for pure TiO₂ and 80% for Nb-TiO₂ to 95% for KBrO₃/Nb-TiO₂. In addition, the nanocomposite with KBrO₃ showed a higher adsorption capacity compared to the TiO₂; the degradation quantity of the dye reached 191 mg for 1 g for the Nb-doped oxide assisted with KBrO₃. However, the degradation quantity of the same dye with the pure TiO₂ was 128 mg for the same time. Finally, the de-colorization of the wastewater containing phenol red in this work confirmed an important interfacial charge between the KBrO₃ and the Nb/TiO₂ nanocomposites.

Author Contributions: Conceptualization, C.A. and N.M.S.; Data curation, N.K.A., C.A., N.A.T. and N.M.S.; Formal analysis, C.A., N.M.A. and N.M.S.; Funding acquisition, N.K.A.; Investigation, C.A. and N.M.S.; Methodology, C.A. and N.M.S.; Supervision, C.A. and N.M.S.; Validation, C.A. and N.M.S.; Visualization, C.A., A.A.A. and N.M.S.; Writing—original draft, C.A. and N.M.S.; Writing—review and editing, N.K.A., C.A., N.M.A., N.A.T., A.A.A. and N.M.S. All authors have read and agreed to the published version of the manuscript.

Funding: This work was supported by the Deanship of Scientific Research, Vice Presidency for Graduate Studies and Scientific Research, King Faisal University, Saudi Arabia [Project No. GRANT 1031].

Conflicts of Interest: The authors declare no conflict of interest.

References

- Xiao, M.; Luo, B.; Lyu, M.; Wang, S.; Wang, L. Photocatalysis: Single-Crystalline Nanomesh Tantalum Nitride Photocatalyst with Improved Hydrogen-Evolving Performance (Adv. Energy Mater. 1/2018). *Adv. Energy Mater.* **2018**, *8*, 1770138. [CrossRef]
- Zhang, L.; Zhao, Z.-J.; Wang, T.; Gong, J. Nano-designed semiconductors for electro- and photoelectro-catalytic conversion of carbon dioxide. *Chem. Soc. Rev.* **2018**, *47*, 5423–5443. [CrossRef]
- Yoon, J.W.; Kim, J.-H.; Jo, Y.-M.; Lee, J.-H. Heterojunction between bimetallic metal-organic framework and TiO₂: Band-structure engineering for effective photoelectrochemical water splitting. *Nano Res.* **2022**, *15*, 8502–8509. [CrossRef]
- Chatterjee, D.; Dasgupta, S. Visible light induced photocatalytic degradation of organic pollutants. *J. Photochem. Photobiol. C Photochem. Rev.* **2005**, *6*, 186–205. [CrossRef]
- Peerakiathajohn, P.; Butburee, T.; Sul, J.-H.; Thaweesak, S.; Yun, J.-H. Efficient and Rapid Photocatalytic Degradation of Methyl Orange Dye Using Al/ZnO Nanoparticles. *Nanomaterials* **2021**, *11*, 1059. [CrossRef]

6. Pozan, G.S.; Isleyen, M.; Gokcen, S. Transition metal coated TiO₂ nanoparticles: Synthesis, characterization and their photocatalytic activity. *Appl. Catal. B Environ.* **2013**, *140–141*, 537–545. [[CrossRef](#)]
7. Tayade, R.J.; Natarajan, T.S.; Bajaj, H.C. Photocatalytic Degradation of Methylene Blue Dye Using Ultraviolet Light Emitting Diodes. *Ind. Eng. Chem. Res.* **2009**, *48*, 10262–10267. [[CrossRef](#)]
8. Mathew, S.; Ganguly, P.; Rhatigan, S.; Kumaravel, V.; Byrne, C.; Hinder, S.J.; Bartlett, J.; Nolan, M.; Pillai, S.C. Cu-Doped TiO₂: Visible light assisted photocatalytic antimicrobial activity. *Appl. Sci.* **2018**, *8*, 2067. [[CrossRef](#)]
9. Verbruggen, S.W.; Keulemans, M.; Filippousi, M.; Flahaut, D.; Van Tendeloo, G.; Lacombe, S.; Martens, J.A.; Lenaerts, S. Plasmonic gold–silver alloy on TiO₂ photocatalysts with tunable visible light activity. *Appl. Catal. B Environ.* **2014**, *156–157*, 116–121. [[CrossRef](#)]
10. Yang, X.; Min, Y.; Li, S.; Wang, D.; Mei, Z.; Liang, J.; Pan, F. Conductive Nb-doped TiO₂ thin films with whole visible absorption to degrade pollutants. *Catal. Sci. Technol.* **2018**, *8*, 1357–1365. [[CrossRef](#)]
11. Ahmed, F.; Kanoun, M.B.; Awada, C.; Jonin, C.; Brevet, P.-F. An Experimental and Theoretical Study on the Effect of Silver Nanoparticles Concentration on the Structural, Morphological, Optical, and Electronic Properties of TiO₂ Nanocrystals. *Crystals* **2021**, *11*, 1488. [[CrossRef](#)]
12. Al Suliman, N.; Awada, C.; Alshoaiibi, A.; Shaalan, N.M. Simple Preparation of Ceramic-Like Materials Based on 1D-Ag_x (x = 0, 5, 10, 20, 40 mM)/TiO₂ Nanostructures and Their Photocatalysis Performance. *Crystals* **2020**, *10*, 1024. [[CrossRef](#)]
13. Awada, C.; Hajlaoui, T.; Al Suliman, N.; Dab, C. Heterogeneous Nanoplasmonic Amplifiers for Photocatalysis and Application: A Theoretical Study. *Catalysts* **2022**, *12*, 771. [[CrossRef](#)]
14. Humayun, M.; Raziq, F.; Khan, A.; Luo, W. Modification strategies of TiO₂ for potential applications in photocatalysis: A critical review. *Green Chem. Lett. Rev.* **2018**, *11*, 86–102. [[CrossRef](#)]
15. Zhang, X.; Song, L.; Zeng, X.; Li, M. Effects of Electron Donors on the TiO₂ Photocatalytic Reduction of Heavy Metal Ions under Visible Light. *Energy Procedia* **2012**, *17*, 422–428. [[CrossRef](#)]
16. Tian, F.; Zhu, R.; Ouyang, F. Synergistic photocatalytic degradation of pyridine using precious metal supported TiO₂ with KBrO₃. *J. Environ. Sci.* **2013**, *25*, 2299–2305. [[CrossRef](#)]
17. Zou, C.; Geng, Q.-J.; Zhu, J.-T.; Jing, C.; Zhong, W.; Hou, Z.-S. Effects of KBr and KI on Photocatalytic Degradation of Dye W-7G with Nano-TiO₂ as Catalyst. *Int. J. Photoenergy* **2021**, *2021*, 6610093. [[CrossRef](#)]
18. Vučić, M.D.R.; Mitrović, J.Z.; Kostić, M.M.; Velinov, N.D.; Najdanović, S.M.; Bojić, D.V.; Bojić, A.L. Heterogeneous photocatalytic degradation of anthraquinone dye Reactive Blue 19: Optimization, comparison between processes and identification of intermediate products. *Water SA* **2020**, *46*, 291–299. [[CrossRef](#)]
19. Almulhem, N.; Awada, C.; Shaalan, N.M. Photocatalytic Degradation of Phenol Red in Water on Nb(x)/TiO₂ Nanocomposites. *Crystals* **2022**, *12*, 911. [[CrossRef](#)]
20. Liu, J.; Xue, D.; Li, K. Single-crystalline nanoporous Nb₂O₅ nanotubes. *Nanoscale Res. Lett.* **2011**, *6*, 138. [[CrossRef](#)]
21. Asiri, A.M.; Al-Amoudi, M.S.; Al-Talhi, T.A.; Al-Talhi, A.D. Photodegradation of Rhodamine 6G and phenol red by nanosized TiO₂ under solar irradiation. *J. Saudi Chem. Soc.* **2011**, *15*, 121–128. [[CrossRef](#)]
22. Daneshvar, N.; Salari, D.; Khataee, A.R. Photocatalytic degradation of azo dye acid red 14 in water on ZnO as an alternative catalyst to TiO₂. *J. Photochem. Photobiol. A Chem.* **2004**, *162*, 317–322. [[CrossRef](#)]
23. Rajamanickam, D.; Shanthi, M. Photocatalytic degradation of an organic pollutant by zinc oxide–solar process. *Arab. J. Chem.* **2016**, *9*, S1858–S1868. [[CrossRef](#)]